Graphene mode-locked multipass-cavity femtosecond Cr⁴⁺: forsterite laser

Sarper Ozharar,[1] Isinsu Baylam,[2,3] M. Natali Cizmeciyan,[2,3] Osman Balci,[4] Ercag Pince,[4]
Coskun Kocabas,[4] and Alphan Sennaroglu[2,3,*]

[1]*College of Arts and Sciences, Bahçeşehir University, Besiktas, Istanbul 34353, Turkey*
[2]*Laser Research Laboratory, Departments of Physics and Electrical-Electronics Engineering, Koç University,
Rumelifeneri, Sariyer, Istanbul 34450, Turkey*
[3]*Koç University Surface Science and Technology Center (KUYTAM), Rumelifeneri, Sariyer, Istanbul 34450, Turkey*
[4]*Bilkent University, Department of Physics, Ankara 06800, Turkey*
*Corresponding author: asennar@ku.edu.tr

We report, for the first time to our knowledge, the use of graphene as a saturable absorber in an energy-scaled femtosecond Cr⁴⁺: forsterite laser. By incorporating a multipass cavity, the repetition rate of the original short resonator was reduced to 4.51 MHz, which resulted in the generation of 100 fs, nearly transform-limited pulses at 1252 nm with a peak power of 53 kW. To the best of our knowledge, this is the highest peak power obtained from a room-temperature, femtosecond Cr⁴⁺: forsterite laser mode locked with a graphene saturable absorber. The corresponding pulse energy was 5.3 nJ with only 24 mW of average output power. The saturation fluence and modulation depth of the GSA were measured to be 25 µJ/cm² and 0.74%, respectively. The nonlinear effects in the Cr⁴⁺: forsterite medium that limit further power scaling were also investigated by using different output couplers.   © 2013 Optical Society of America

OCIS codes: (140.3580) Lasers, solid-state; (140.4050) Mode-locked lasers; (140.5680) Rare earth and transition metal solid-state lasers; (140.7090) Ultrafast lasers; (140.3600) Lasers, tunable.
http://dx.doi.org/10.1364/JOSAB.30.001270

1. INTRODUCTION

A collection of carbon atoms can have a wide variety of physical, mechanical, optical, and electrical properties based on their geometrical form. These crystalline allotropes of carbon are named based on their dimensions as fullerene (zero-dimensional form), carbon nanotube (one-dimensional form), graphene [two-dimensional (2D) form], graphite, and diamond (three-dimensional forms). Each allotrope has its own unique properties and different uses [1–3]. Among these, graphene is chronologically the latest allotrope that has been produced.

Graphene is the 2D arrangement of carbon atoms in a hexagonal honeycomb lattice. Each carbon atom is connected to three other carbon atoms by sp^2 hybridization. Graphene has been explored in a diverse range of potential applications in electronics (flexible electronics, high-frequency transistors), biomedical applications [4], and optics (fast photodetectors, transparent electrodes [5]). The optical properties of graphene are dominated by its dispersion relation, given by [6]

$$E^{\pm} = \pm \hbar \nu_F |k|, \qquad (1)$$

where k is the wave vector of the electron, ν_F is the group velocity of the electron, and $\hbar$ is $h/2\pi$ (h = Planck's constant). According to Eq. (1), the band energy varies linearly with the wave vector and defines the valence and conduction bands of graphene as two cones with zero band-gap energy in between, referred to as the Dirac cones. Due to this unique zero band-gap energy and the linear dispersion

relation, the absorption of a single-layer graphene is nearly independent of wavelength and can be expressed as [7]

$$A = \pi \alpha \approx 2.3\%, \qquad (2)$$

where α is the fine structure constant. Therefore, one can estimate the number of graphene layers by measuring the linear absorption of a sample.

It has also been shown that graphene can be used as an effective saturable absorber in order to initiate the mode-locked operation of lasers emitting in the 800–2500 nm wavelength range [8–12]. As an example, peak powers as high as 77 kW have been generated from a graphene mode-locked femtosecond Ti:sapphire oscillator [9]. Among the tunable solid-state lasers operating in the near infrared, the Cr⁴⁺: forsterite gain medium has been widely used in the generation of ultrashort optical pulses near 1.3 µm for several potential biomedical applications. The operating wavelength range of the Cr⁴⁺: forsterite laser is long enough to have less scattering in biological tissue in comparison with neodymium or Ti:sapphire lasers. At the same time, it is below the strong absorption band of water, making the source ideal for biomedical imaging techniques, such as optical coherence tomography or multiphoton microscopy [13–15]. To date, femtosecond pulse generation in Cr⁴⁺: forsterite has been achieved using additive-pulse mode locking [16], Kerr-lens mode (KLM) locking [17–19], and saturable absorber mode locking with different saturable absorbers, such as semiconductor saturable absorber mirrors [20], semiconductor doped

glasses [21], single-walled carbon nanotubes [22, 23], and graphene [10], to name a few. For example, in previous studies performed with graphene mode-locked Cr^{4+}: forsterite lasers, pulses with as high as 33 kW of peak power were produced [10]. Furthermore, mode-locked operation has also been obtained in extended-cavity or multipass-cavity (MPC) configurations [24–26] to scale the output pulse energies from megahertz repetition rate Cr^{4+}: forsterite oscillators up to 81 nJ [26]. One important advantage of the MPC architecture is that pulse energy scaling is achieved at considerably lower average powers and, hence, thermal effects are also significantly reduced [14].

In this work, we have successfully employed graphene as an intracavity saturable absorber in the generation of mode-locked pulses from an MPC Cr^{4+}: forsterite laser. The resonator produced 5.3 nJ pulses at the center wavelength of 1252 nm with a duration of 100 fs. The corresponding peak power of 53 kW is the highest obtained to date from a room-temperature Cr^{4+}: forsterite laser mode locked with a graphene saturable absorber (GSA). These results show the potential of GSAs as robust saturable absorbers for mode locking of energy-scaled femtosecond solid-state lasers.

2. PRODUCTION AND CHARACTERIZATION OF GRAPHENE

There are many different methods for fabricating few- or single-layer graphene, such as micromechanical exfoliation, liquid-phase exfoliation, and chemical vapor deposition [5]. The graphene samples, used in this study, were synthesized on copper foils with chemical vapor deposition [27]. The copper foils were placed in a quartz chamber and heated to 1000°C under a flow of hydrogen and argon. We annealed the foils at 1000°C for 20 min. before the growth. A mixture of methane and hydrogen (7 sccm CH_4 and 7 sccm H_2) was used as a reaction gas. The chamber pressure was kept at 300 mTorr during the growth. The growth was terminated by stopping the flow of methane and then the chamber was cooled back to room temperature. After the growth, the graphene layers were transfer printed on quartz substrate [28]. The copper foils were spin coated with a thin layer of photoresist (PR, AZ5214). A flat elastomeric stamp [polydimethylsiloxane (PDMS)] was placed on the PR layer and the copper foil was etched by 1 M iron chloride solution. After the etching process, the PR layer with graphene remains on the PDMS stamp. The stamp was applied on quartz substrates and heated to 80°C to release the PR. After removing the stamp, the PR layer was removed in acetone.

Raman spectrum measurements are also commonly used in the characterization of graphene samples since they give information not only about the number of layers but also
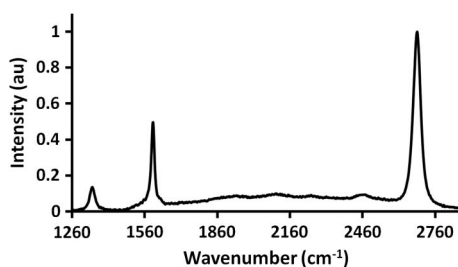
about possible structural defects in the graphene layers [29]. In this method, the sample is illuminated with a monochromatic light source and the amount of energy lost due to the excitation of vibrational modes (phonons) is determined by measuring the wavelength shift of the scattered light. The Raman spectrum of the graphene samples used in the experiment, excited at 532 nm, showed characteristic G band and 2D band peaks at 1580 cm^{-1} and at 2700 cm^{-1}, respectively, as seen in Fig. 1. The third peak at 1350 cm^{-1} is the D band.

Ideally, in a sample with no defects, this peak will not be present [30]. Therefore, its relative height with respect to the height of the G band (D/G) is a measure of the amount of defects on the sample. Also, the full width at half-maximum (FWHM) of the 2D band becomes broader as the number of graphene layers increases. Therefore, both of these parameters are used to evaluate the merit of the graphene sample [29]. In our measurements, the D/G value was calculated to be 0.135 and the FWHM of the 2D band was measured to be 38 cm^{-1}, confirming the formation of a single-layer graphene with a low fraction of defects on the quartz substrate [29,30].

Ultrafast relaxation dynamics of the graphene sample were further investigated with a commercial time-resolved pump-probe spectrometer (HELIOS, Ultrafast Systems). As a pump source, we used the output of a tunable optical parametric amplifier (TOPAS, Spectra Physics) at 400 nm, which was seeded with 2 mJ, 100 fs pulses at a pulse repetition frequency of 1 kHz from a commercial Ti:sapphire chirped-pulse amplifier (Spitfire ACE, Newport-Spectra Physics). The sample was probed with a broadband near-infrared continuum, spanning from 900 to 1600 nm. A typical time-resolved transmission response of the single-layer graphene at 1250 nm is shown in Fig. 2. Two distinct relaxation pathways with fast and slow decay time occur during recovery.

As has been identified in earlier studies, the fast transition of excited carriers is due to the carrier–carrier intraband collisions and phonon emission, whereas the slow transition occurs as a result of the cooling of hot phonons and electron-hole interband scattering [31]. By fitting a decaying biexponential function to the data, as plotted in Fig. 2, we determined the fast and slow time constants as 297 fs and 1.56 ps, respectively.

The saturation characteristics of the GSA were also measured with the pump-probe setup. Figure 3 shows the

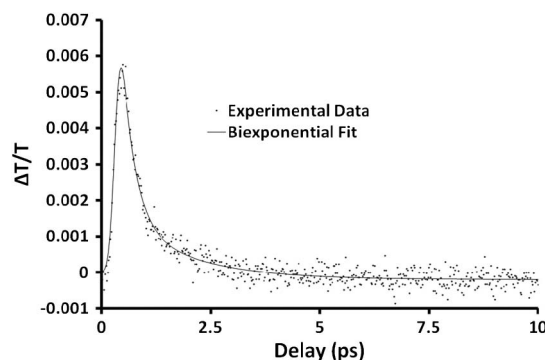

Fig. 1.   Measured Raman spectrum of the GSA.

Fig. 2.   Variation of the fractional transmission change at 1250 nm as a function of delay for the single-layer GSA during time-resolved pump-probe measurements.
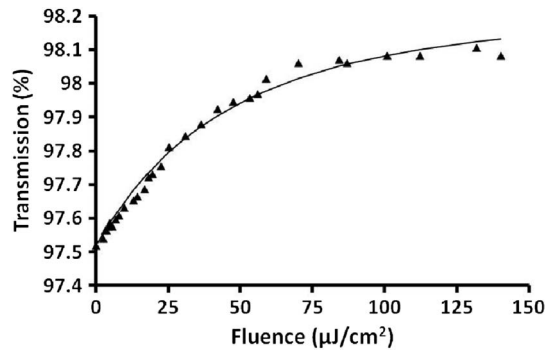
Fig. 3.   Measured variation of the transmission at 1250 nm as a function of the pump fluence for the single-layer GSA.

measured change in the transmission of the single-layer graphene absorber as a function of pump fluence. The saturation fluence and the modulation depth were determined to be 25 $\mu J/cm^2$ and 0.74%, respectively.

3. EXPERIMENTAL SETUP

In order to explore the performance of the GSA in an energy-scaled resonator, we built a Cr^{4+}: forsterite laser containing a q-preserving MPC [32]. The MPC configuration enables the generation of high-peak-power pulses at low average power by reducing the repetition rate of the mode-locked pulse train. The initial laser cavity had a standard x-cavity design, extending between the end mirrors M5 (high reflector) and M10 [output coupler (OC)] as can be seen in Fig. 4. The MPC section was introduced into the laser cavity by removing M5. The MPC consisted of two notched high reflectors (M6 with $R = 4$ m and the flat high reflector M7), separated by 165 cm. The injected beam completes nine roundtrips between M6 and M7. The flat high reflector M8 and the curved high reflector M9 ($R = 2$ m) reflected the beam back into the short cavity. The distance traveled by the beam after exiting the MPC up to the curved retro-reflector M9 was equal to the separation of the MPC mirrors M6 and M7. This guarantees that the MPC configuration is q preserving. In other words, the beam returning from the MPC into the original short cavity has the same q parameter as the incident beam so that the spot-size distribution inside the gain medium of the original short cavity is not modified. The MPC extension provided an additional effective path length of 59.4 m to the original cavity.
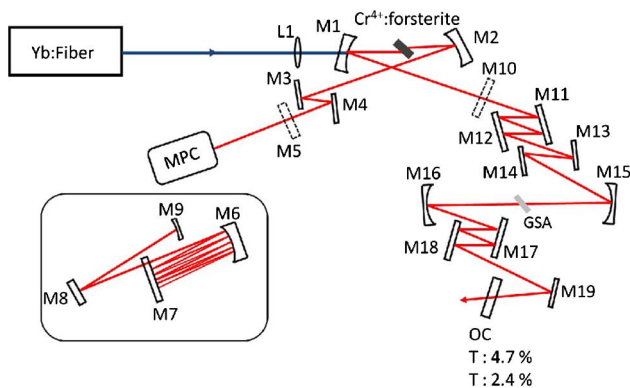
On the OC side of the cavity, additional optics were included to house the GSA and to control the net cavity dispersion. In particular, four flat Gires–Tournois interferometer (GTI) mirrors (M11, M12, M17, and M18), each having a group delay dispersion (GDD) of -250 fs^2 per bounce and three flat dispersion-compensating mirrors (DCMs) (M13, M14, and M19), each having a GDD of -150 fs^2 per bounce, were added into the cavity. The beam path was aligned such that the circulating beam reflected off four times from the GTI mirrors and two times from the DCM mirrors in each roundtrip. These GTI mirrors and DCMs together with other cavity components (MPC, $+360$ fs^2; gain crystal, $+800$ fs^2; air, $+794$ fs^2; quartz substrate, $+7$ fs^2; other dispersive mirrors, -1500 fs^2) introduced a net intracavity GDD of around -4440 fs^2 in one roundtrip. The GSA was further positioned between the curved high reflectors M15 and M16, each with a radius of curvature of 500 mm. The overall cavity containing the short cavity, the MPC extension, dispersion control optics, and the intracavity focusing mirrors for the GSA had a total optical path length of 66.5 m. The corresponding pulse repetition frequency became 4.51 MHz. To reduce phase instabilities arising from air currents, the MPC setup was also covered with a Plexiglass enclosure.

The 20 mm long Brewster-cut Cr^{4+}: forsterite crystal was kept at a constant temperature of 20°C by water cooling and was pumped with a continuous-wave (cw) Yb: fiber laser at 1064 nm. The pump beam was focused down to a beamwaist of approximately 30 μm with an input converging lens (L1) with a focal length of 20 cm.

In the experiments, two different OCs with intensity transmission of 4.7% and 2.4% were used to test the operation of the GSA at different intracavity power levels. Both OCs were flat and used as end mirrors, as shown in Fig. 4. In order to saturate the absorption band of the graphene sample with sufficient fluence, an intracavity beamwaist was formed using two additional curved mirrors (M15 and M16, each with ROC = 500 mm), as described above. The estimated beamwaist on the GSA was 97 μm. The graphene sample was placed near the center of the M15–M16 separation, and its position was adjusted to optimize the mode-locked operation. In this configuration, a saturation fluence of 382 $\mu J/cm^2$ (339 $\mu J/cm^2$) was obtained on the GSA by using the 4.7% (2.4%) OC.

Excluding the MPC part, there are three beamwaists in the laser cavity: inside the gain crystal, near the location of the
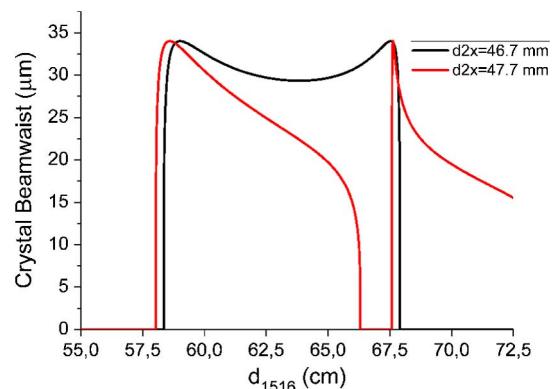

Fig. 4.   Experimental setup of the MPC Cr^{4+}: forsterite laser containing the GSA.

Fig. 5.   Calculated variation of the beamwaist inside the crystal as a function of the distance between M15 and M16 (d_{1516}) for two different values of d_{2x}.

GSA between M15 and M16, and on the OC. As expected, the size of these beamwaists cannot be optimized independently by changing the cavity parameters, such as the mirror positions. The stability curve in Fig. 5 shows the beamwaist size inside the crystal as a function of the distance between the focusing mirrors M15 and M16 (d_{1516}), for two different values of the distance between the crystal and M2 (d_{2x}). As seen from this stability curve, when d_{2x} is equal to 47.7 mm, the beamwaist inside the crystal is extremely sensitive to d_{1516}. However, when d_{2x} is changed to 46.6 mm, the beamwaist is relatively constant for different values of d_{1516}. Furthermore, the laser operation was more stable and cavity optimization became easier.

Another important cavity parameter that needs to be optimized is the amount of intracavity dispersion. The dispersion contribution of various intracavity components was discussed above. Based on the soliton-area theorem, the pulse energy is proportional to the intracavity dispersion when the laser operates in the solitary region as given by [33]

$$W\tau_p = 1.76\frac{|D|\lambda A_{\text{eff}}}{\pi n_2 l_g}. \tag{3}$$

Here, W is the intracavity pulse energy, τ_p is the FWHM pulse duration, D is the roundtrip GDD, λ is the wavelength, A_{eff} is the effective cross-sectional area of the laser beam inside the gain medium, l_g is length of the gain medium, and n_2 is the nonlinear refractive index of the gain medium. Since the inclusion of the MPC scales up the pulse energy during mode-locked operation, additional intracavity dispersion is necessary to balance the nonlinearities arising from self-phase modulation, as can be seen from Eq. (3). Mode-locking data together with Eq. (3) were used to estimate the nonlinear index n_2 for the Cr^{4+}: forsterite gain medium as discussed in the next section.

In the experiments, inclusion of the GSA easily initiated mode-locked operation of the MPC Cr^{4+}: forsterite laser and a stable train of femtosecond pulses could be generated. The output of the laser was split into three beams in order to monitor the spectrum, the autocorrelation, and the pulse train simultaneously during mode-locked operation.

4. RESULTS AND DISCUSSION

Figure 6 shows the power efficiency curves of the laser with and without the GSA for different OCs. The insertion
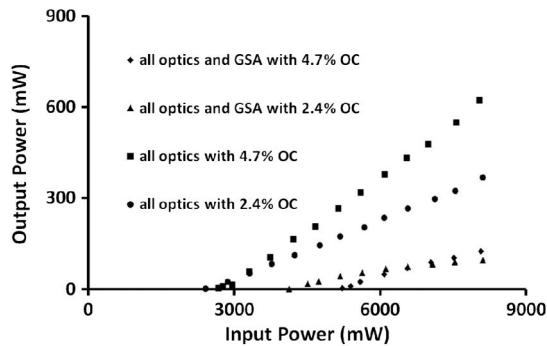

Fig. 6.   Power efficiency curves of the laser resonator with and without the GSA at two different output coupling levels (GSA, graphene saturable absorber; and OC, output coupler).
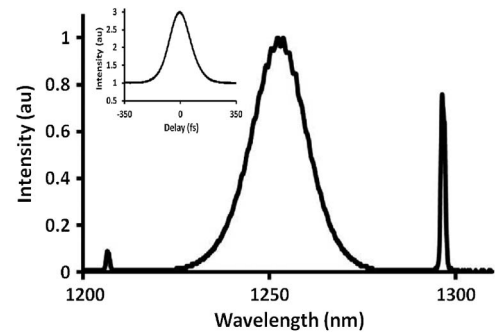

Fig. 7.   Mode-locked spectrum and collinear autocorrelation trace (inset) of the graphene mode-locked MPC Cr^{4+}: forsterite laser with the 4.7% OC.

loss of the GSA can be determined from the lasing threshold data obtained for different configurations, using the equations [34]

$$(P_P)_{\text{th}} = A(L + T) \tag{4}$$

and

$$\frac{(P_P)_{\text{th1}}}{(P_P)_{\text{th2}}} = \frac{L_1 + T_1}{L_2 + T_2}. \tag{5}$$

Above, $(P_P)_{\text{th1,2}}$ is the threshold pump power for two different configurations designated as "1" and "2", A is a constant, $L_{1,2}$ is the corresponding total roundtrip passive loss of the resonator, and $T_{1,2}$ is the respective transmission of the OC. In this particular case, configurations 1 and 2 correspond to the cases without and with the GSA in the cavity, respectively. Therefore, L_2 is given by

$$L_2 = L_1 + L_{\text{GSA}}. \tag{6}$$

From the threshold analysis of the composite cavity operated with 4.7% and 2.4% OCs, the average single-pass optical loss of the GSA was estimated to be around 3.15%. This result confirms the existence of a single layer of graphene on the quartz substrate. The additional loss of 0.85% is probably due to the imperfections on the quartz substrate.

The mode-locked spectra and the autocorrelation traces of the laser with the 4.7% and 2.4% OCs are shown in Figs. 7 and 8, respectively. In each case, Kelly sidebands were observed on both sides of the pulse spectrum [35]. It was further found that the intensity of the Kelly sidebands could
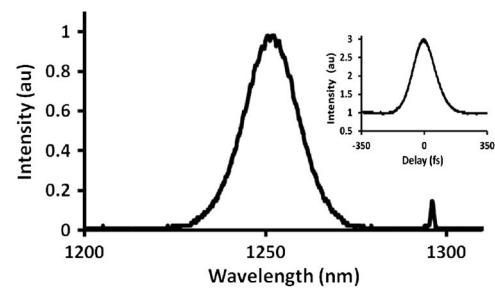

Fig. 8.   Mode-locked spectrum and collinear autocorrelation trace (inset) of the graphene mode-locked MPC Cr^{4+}: forsterite laser with the 2.4% OC.
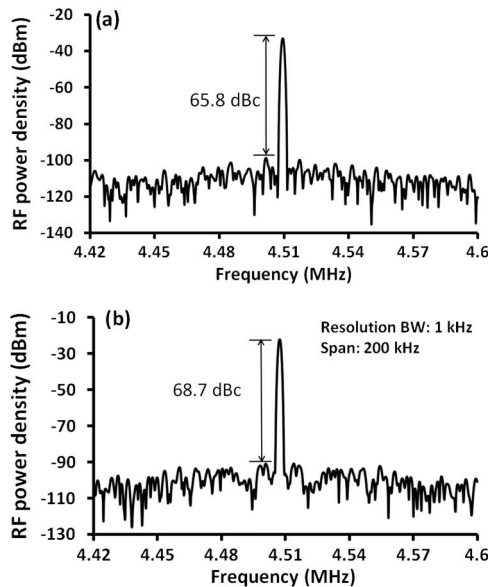
Fig. 9.   RF spectra of the graphene mode-locked MPC Cr^{4+}: forsterite laser operated with (a) the 2.4% and (b) the 4.7% OC.

be varied by changing the focusing inside the Cr^{4+}: forsterite gain medium.

With the 2.4% OC, the laser produced mode-locked pulses with an output energy of 2.4 nJ. The pulse duration (FWHM) was further measured to be 94 fs by assuming a sech^2 intensity profile. The corresponding spectral bandwidth at 1252 nm was 18 nm, giving a time-bandwidth product of 0.32. In the case of the 4.7% OC, the output pulse energy increased to 5.3 nJ. The pulse duration and the spectral bandwidth (at 1252 nm) were measured to be 100 fs and 17.6 nm, respectively (corresponding time-bandwidth product = 0.33). In both cases, the generated pulses were nearly transform limited.

With both OCs, the output of the graphene mode-locked MPC Cr^{4+}: forsterite laser was further photodetected and analyzed with an RF spectrum analyzer to investigate the mode-locking stability. The resulting RF spectra of the fundamental tone are shown in Figs. 9(a) and 9(b) for the 2.4% and 4.7% OCs, respectively. The sideband noise level was determined to be 65.8 dB (for the 2.4% OC) and 68.7 dB (for the 4.7% OC) below the carrier at a resolution bandwidth of 1 kHz.

Figure 10 shows the measured cw output power of the composite Cr^{4+}: forsterite laser (without the GSA) at the input pump power of 7.1 W as a function of the OC transmission. The estimated optimum output coupling was around 6%.
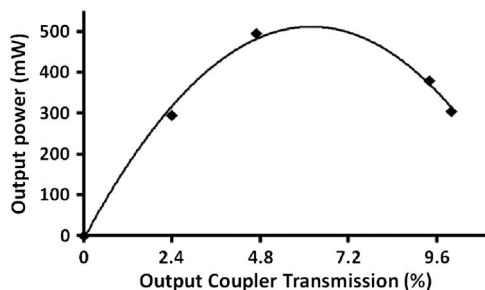

Fig. 10.   Measured CW output power of the composite Cr^{4+}: forsterite laser (without the GSA) at the input pump power of 7.1 W as a function of the OC transmission.

However, inclusion of the GSA introduced an additional roundtrip loss of approximately 6.3% and with the available optics, the graphene mode-locked MPC Cr^{4+}: forsterite laser could not be operated with output coupling larger than 4.7%. In our previous work, where a single-walled carbon nanotube saturable absorber (SWCNT-SA) was used to initiate mode locking, the resonator could be operated with an output coupling as high as 9.4%. Since the intracavity energy during stable mode-locked operation was similar in both experiments, lower output pulse energy was extracted in this study in comparison with what was obtained from the SWCNT-SA mode-locked MPC Cr^{4+}: forsterite laser in [23].

At the maximum pumping level, the resonator with the 4.7% and 2.4% OCs produced output powers of 24 and 11 mW, respectively, corresponding to output peak powers of 53 kW (4.7%) and 25 kW (2.4%) at the pulse repetition frequency of 4.51 MHz. The corresponding maximum intracavity peak power during single-pulse operation was 1.13 MW (4.7% OC) and 1.06 MW (2.4% OC).

Any further increase in the pump power resulted in temporal and spectral instabilities, such as multipulsing and generation of a CW peak on the mode-locked spectrum. This is because the laser cavity did not have sufficient dispersion to balance the nonlinearities at higher intracavity power levels. The main source for the intracavity nonlinearity originates from the Cr^{4+}: forsterite crystal. By using Eq. (3), the nonlinear refractive index (n_2) of the gain crystal was estimated to be $n_2 = 11.83 \pm 0.2 \cong 10^{-20}$ m^2/W, in good agreement with our previously reported n_2 value of $9.36 \cong 10^{-20}$ m^2/W [23].

From the nonlinear refractive index of the gain medium, we can also estimate the critical intracavity power for self focusing from [36]

$$P_{\mathrm{cr}} = \frac{a\lambda^2}{8\pi n_0 n_2}, \qquad (7)$$

where a is a dimensionless correction factor taken as 3.77, n_0 and n_2 are the linear and nonlinear refractive indices of the medium, and λ is the central wavelength of the laser spectrum. The critical power gives an order-of-magnitude estimate for the maximum intracavity peak powers that can be attained before multipulsing instabilities begin due to the nonlinear effects. Based on the average n_2 value determined in this study, the critical power for self focusing was determined to be 1.21 MW for the Cr^{4+}: forsterite medium, which is in good agreement with the maximum peak power values of 1.13 MW (4.7% OC) and 1.06 MW (2.4% OC) measured in our experiments.

5. CONCLUSIONS

In conclusion, we have successfully employed a GSA to initiate the mode-locked operation of an energy-scaled femtosecond Cr^{4+}: forsterite laser. In the experiments, the GSA sample was grown on a quartz substrate by using the CVD technique and was then characterized using Raman and pump-probe spectroscopy. The GSA sample was then placed inside an MPC Cr^{4+}: forsterite laser operating at a pulse repetition rate of 4.51 MHz. Using the 4.7% OC, nearly transform-limited pulses with a duration of 100 fs and a pulse energy of 5.3 nJ were produced near 1252 nm. To our knowledge, the peak power of 53 kW obtained with the 4.7% OC, is the highest

peak power obtained to date from a GSA mode-locked femto-second Cr^{4+}: forsterite laser at room temperature. Further-more, the maximum peak intracavity powers obtained with the 2.4% and 4.7% OCs were close to the estimated critical power for self focusing, suggesting that in this particular case, self focusing in the Cr^{4+}: forsterite gain medium is the major factor that limits further power scaling.

ACKNOWLEDGMENTS

REFERENCES

1. S. Iijima, "Helical microtubules of graphitic carbon," Nature **354**, 56–58 (1991).
2. H. W. Kroto, J. R. Heath, S. C. Obrien, R. F. Curl, and R. E. Smalley, "C-60—Buckminsterfullerene," Nature **318**, 162–163 (1985).
3. K. S. Novoselov, A. K. Geim, S. V. Morozov, D. Jiang, Y. Zhang, S. V. Dubonos, I. V. Grigorieva, and A. A. Firsov, "Electric field effect in atomically thin carbon films," Science **306**, 666–669 (2004).
4. K. S. Novoselov, V. I. Fal'ko, L. Colombo, P. R. Gellert, M. G. Schwab, and K. Kim, "A roadmap for graphene," Nature **490**, 192–200 (2012).
5. F. Bonaccorso, Z. Sun, T. Hasan, and A. C. Ferrari, "Graphene photonics and optoelectronics," Nat. Photonics **4**, 611–622 (2010).
6. A. H. Castro Neto, F. Guinea, N. M. R. Peres, K. S. Novoselov, and A. K. Geim, "The electronic properties of graphene," Rev. Mod. Phys. **81**, 109–162 (2009).
7. A. B. Kuzmenko, E. V. Heumen, F. E. Carbone, and A. D. D. Marel, "Universal optical conductance of graphite," Phys. Rev. Lett. **100**, 117401 (2008).
8. Q. L. Bao, H. Zhang, Y. Wang, Z. H. Ni, Y. L. Yan, Z. X. Shen, K. P. Loh, and D. Y. Tang, "Atomic-layer graphene as a saturable absorber for ultrafast pulsed lasers," Adv. Funct. Mater. **19**, 3077–3083 (2009).
9. I. H. Baek, H. W. Lee, S. Bae, B. H. Hong, Y. H. Ahn, D. I. Yeom, and F. Rotermund, "Efficient mode-locking of sub-70 fs Ti:sapphire laser by graphene saturable absorber," Appl. Phys. Express **5**, 032701 (2012).
10. W. B. Cho, J. W. Kim, H. W. Lee, S. Bae, B. H. Hong, S. Y. Choi, I. H. Baek, K. Kim, D. I. Yeom, and F. Rotermund, "High-quality, large-area monolayer graphene for efficient bulk laser mode-locking near 1.25 μm," Opt. Lett. **36**, 4089–4091 (2011).
11. J. Ma, G. Q. Xie, P. Lv, W. L. Gao, P. Yuan, L. J. Qian, H. H. Yu, H. J. Zhang, J. Y. Wang, and D. Y. Tang, "Graphene mode-locked femtosecond laser at 2 μm wavelength," Opt. Lett. **37**, 2085–2087 (2012).
12. M. N. Cizmeciyan, J. W. Kim, S. Bae, B. H. Hong, F. Rotermund, and A. Sennaroglu, "Graphene mode-locked femtosecond Cr:ZnSe laser at 2500 nm," Opt. Lett. **38**, 341–343 (2013).
13. G. J. Tearney, M. E. Brezinski, B. E. Bouma, S. A. Boppart, C. Pitris, J. F. Southern, and J. G. Fujimoto, "In vivo endoscopic optical biopsy with optical coherence tomography," Science **276**, 2037–2039 (1997).
14. V. V. Yakovlev, A. Ivanov, and V. Shcheslavskiy, "High-energy femtosecond Cr^{4+}: forsterite oscillators and their applications in biomedical and material sciences," Appl. Phys. B **74**, S145–S152 (2002).
15. C. K. Sun, C. C. Chen, S. W. Chu, T. H. Tsai, Y. C. Chen, and B. L. Lin, "Multiharmonic-generation biopsy of skin," Opt. Lett. **28**, 2488–2490 (2003).
16. A. Sennaroglu, T. J. Carring, and C. R. Pollock, "Femtosecond pulse generation by using an additive-pulse mode-locked chromium-doped forsterite laser operated at 77 K," Opt. Lett. **17**, 1216–1218 (1992).
17. A. Seas, V. Petricevic, and R. R. Alfano, "Self-mode-locked chromium-doped forsterite laser generates 50 fs pulses," Opt. Lett. **18**, 891–893 (1993).
18. Y. Pang, V. Yanovsky, F. Wise, and B. I. Minkov, "Self-mode-locked Cr:forsterite laser," Opt Lett **18**, 891–893 (1993).
19. C. Chudoba, J. G. Fujimoto, E. P. Ippen, H. A. Haus, U. Morgner, F. X. Kaertner, V. Scheuer, G. Angelow, and T. Tschudi, "All-solid-state Cr:forsterite laser generating 14 fs pulses at 1.3 μm," Opt. Lett. **26**, 292–294 (2001).
20. Z. G. Zhang, K. Torizuka, T. Itatani, K. Kobayashi, T. Sugaya, and T. Nakagawa, "Femtosecond Cr:forsterite laser with mode lock-ing initiated by a quantum-well saturable absorber," IEEE J. Quantum Electron. **33**, 1975–1981 (1997).
21. R. P. Prasankumar, C. Chudoba, J. G. Fujimoto, P. Mak, and M. F. Ruane, "Self-starting mode locking in a Cr : forsterite laser by use of non-epitaxially-grown semiconductor-doped silica films," Opt. Lett. **27**, 1564–1566 (2002).
22. W. B. Cho, J. H. Yim, S. Y. Choi, S. Lee, U. Griebner, V. Petrov, and F. Rotermund, "Mode-locked self-starting Cr:forsterite laser using a single-walled carbon nanotube saturable absorber," Opt. Lett. **33**, 2449–2451 (2008).
23. I. Baylam, S. Ozharar, H. Cankaya, S. Y. Choi, K. Kim, F. Rotermund, U. Griebner, V. Petrov, and A. A. Sennaroglu, "Energy scaling of a carbon nanotube saturable absorber mode-locked femtosecond bulk laser," Opt. Lett. **37**, 3555–3557 (2012).
24. V. Shcheslavskiy, V. V. Yakovlev, and A. Ivanov, "High-energy self-starting femtosecond Cr^{4+}:Mg_2SiO_4 oscillator operating at a low repetition rate," Opt. Lett. **26**, 1999–2001 (2001).
25. H. Cankaya, J. G. Fujimoto, and A. Sennaroglu, "Low-threshold, 12 MHz, multipass-cavity femtosecond Cr^{4+}: forsterite laser," Laser Phys. **19**, 281–284 (2009).
26. H. Cankaya, A. Sennaroglu, and S. Akturk, "Direct generation of 81 nJ pulses and external compression to a subpicosecond regime with a 4.9 MHz chirped-pulse multipass-cavity Cr(4+): forsterite oscillator," Opt. Lett. **36**, 1572–1574 (2011).
27. X. S. Li, W. W. Cai, J. H. An, S. Kim, J. Nah, D. X. Yang, R. Piner, A. Velamakanni, I. Jung, E. Tutuc, S. K. Banerjee, L. Colombo, and R. S. Ruoff, "Large-area synthesis of high-quality and uni-form graphene films on copper foils," Science **324**, 1312–1314 (2009).
28. O. Salihoglu, S. Balci, and C. Kocabas, "Plasmon-polaritons on graphene-metal surface and their use in biosensors," Appl. Phys. Lett. **100**, 213110 (2012).
29. A. C. Ferrari, J. C. Meyer, V. Scardaci, C. Casiraghi, M. Lazzeri, F. Mauri, S. Piscanec, D. Jiang, K. S. Novoselov, S. Roth, and A. K. Geim, "Raman spectrum of graphene and graphene layers," Phys. Rev. Lett. **97**, 187401 (2006).
30. A. Reina, X. Jia, J. Ho, D. Nezich, H. Son, V. Bulovic, M. S. Dresselhaus, and A. J. Kong, "Large area, few-layer graphene films on arbitrary substrates by chemical vapor deposition," Nano Lett. **9**, 30–35 (2008).
31. J. M. Dawlaty, S. Shivaraman, M. Chandrashekhar, F. Rana, and M. G. Spencer, "Measurement of ultrafast carrier dynamics in epitaxial graphene," Appl. Phys. Lett. **92**, 042116 (2008).
32. A. Sennaroglu, A. M. Kowalevicz, E. P. Ippen, and J. G. Fujimoto, "Compact femtosecond lasers based on novel multi-pass cavities," IEEE J. Quantum Electron. **40**, 519–528 (2004).
33. H. A. Haus, "Mode-locking of lasers," IEEE J. Sel. Top. Quantum Electron. **6**, 1173–1185 (2000).
34. A. Sennaroglu, *Photonics and Laser Engineering: Principles, Devices, and Applications* (McGraw-Hill, 2010).
35. S. M. J. Kelly, "Characteristic side-band instability of periodically amplified average soliton," Electron. Lett. **28**, 806–807 (1992).
36. D. Huang, M. Ulman, L. H. Acioli, H. A. Haus, and J. G. Fujimoto, "Self-focusing-induced saturable loss for laser mode-locking," Opt. Lett. **17**, 511–513 (1992).